Turbulence within Rain-Formed Fresh Lenses during the SPURS-2 Experiment

SUNEIL IYER[a] AND KYLA DRUSHKA[a]

[a] *Applied Physics Laboratory and School of Oceanography, University of Washington, Seattle, Washington*

(Manuscript received 8 December 2020, in final form 11 March 2021)

ABSTRACT: Observations of salinity, temperature, and turbulent dissipation rate were made in the top meter of the ocean using the ship-towed Surface Salinity Profiler as part of the second Salinity Processes in the Upper Ocean Regional Study (SPURS-2) to assess the relationships between wind, rain, near-surface stratification, and turbulence. A wide range of wind and rain conditions were observed in the eastern tropical Pacific Ocean near 10°N, 125°W in summer–autumn 2016 and 2017. Wind was the primary driver of near-surface turbulence and the mixing of rain-formed fresh lenses, with lenses generally persisting for hours when wind speeds were under 5 $\mathrm{m\,s^{-1}}$ and mixing away immediately at higher wind speeds. Rain influenced near-surface turbulence primarily through stratification. Near-surface stratification caused by rainfall or diurnal warming suppressed deeper turbulent dissipation rates when wind speeds were under 3 $\mathrm{m\,s^{-1}}$. In one case with 4–5 $\mathrm{m\,s^{-1}}$ winds, rain-induced stratification enhanced dissipation rates within the stratified layer. At wind speeds above 7–8 $\mathrm{m\,s^{-1}}$, strong stratification was not observed in the upper meter during rain, indicating that rain lenses do not form at wind speeds above 8 $\mathrm{m\,s^{-1}}$. Raindrop impacts enhanced turbulent dissipation rates at these high wind speeds in the absence of near-surface stratification. Measurements of air–sea buoyancy flux, wind speed, and near-surface turbulence can be used to predict the presence of stratified layers. These findings could be used to improve model parameterizations of air–sea interactions and, ultimately, our understanding of the global water cycle.

KEYWORDS: Ocean; Turbulence; Atmosphere-ocean interaction; Rainfall; Surface layer; Salinity

1. Introduction

Small-scale turbulent processes are a crucial part of the pathway by which freshwater from rainfall is incorporated into the salinity structure of the ocean. A primary goal of the second Salinity Processes in the Upper Ocean Regional Study (SPURS-2) is to understand the processes that influence upper-ocean salinity at a variety of spatial and temporal scales (Lindstrom et al. 2019). The present work contributes to this objective as an analysis of the relationships between rain, wind, near-surface stratification, and turbulent mixing. The data collected during the SPURS-2 field campaign are from a region (10°N, 125°W) within the eastern Pacific summer intertropical convergence zone (ITCZ) that receives a large amount of precipitation and has a relatively low sea surface salinity (Figs. 1 and 2). An offset exists between the locations of highest precipitation and lowest salinity (SPURS-2 Planning Group 2015), highlighting the importance of near-surface mixing and advection, in addition to precipitation, for determining the salinity structure. Ocean salinities respond to changes in the global climate and water cycle (Boyer et al. 2005; Durack et al. 2012; Durack 2015), so understanding the processes that contribute to ocean salinity variability is critical. Furthermore, rain is generally parameterized as a surface flux (Fairall et al. 1996) in models where the resolution in the upper layers may be too coarse to resolve very near surface stratification, despite the importance of rain to the surface ocean structure in regions such as the ITCZ. Our analysis evaluates how rainfall influences the surface ocean, which will potentially lead to an improved understanding of the processes that are parameterized in models and the impacts of climate change on the global water cycle.

The present study utilizes observations of salinity and turbulent mixing at horizontal scales of one to tens of kilometers in the upper 1 m of the ocean to gain insight into the processes that create low surface salinities in rainy tropical regions of the ocean. In the eastern tropical Pacific, rain events are frequent, have spatial scales on the order of one to hundreds of kilometers, and are often accompanied by either wind bursts or significant drops in wind speed (Yuter and Houze 2000; Wijesekera et al. 2005; Cifelli et al. 2007, 2008). This is typical of rain events over the tropical ocean (Nesbitt et al. 2006). Because of its location in the ITCZ, the SPURS-2 site is an ideal location to study the relationships between rain, wind, and near-surface mixing.

2. Background, data, and methods

When rain falls on the ocean, the salinity decreases and low density layers of relatively freshwater can form near the surface (Katsaros and Buettner 1969; Price 1979; Tomczak 1995; Wijesekera et al. 1999; Asher et al. 2014; Walesby et al. 2015; Drushka et al. 2016; ten Doeschate et al. 2019; Reverdin et al. 2020). We refer to these fresh anomalies as fresh lenses. Fresh lenses are generally short lived, persisting for minutes to several hours until they are advected away or mixed by wind- and wave-driven turbulence or nighttime convection (Brainerd and Gregg 1997; Wijesekera et al. 1999; Drushka et al. 2016; Reverdin et al. 2020). Salinity and temperature within rain-formed fresh lenses are affected by rain rate, the duration of

Denotes content that is immediately available upon publication as open access.

Corresponding author: Suneil Iyer, iyersk@uw.edu

DOI: 10.1175/JPO-D-20-0303.1

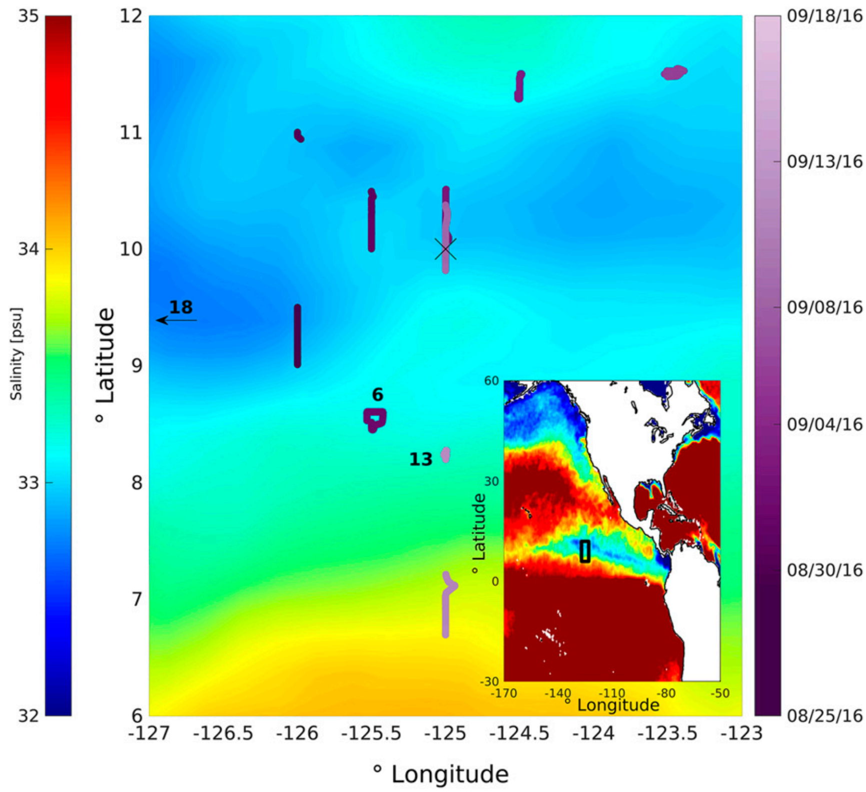

FIG. 1. SSP deployments during the 2016 SPURS-2 cruise. The purple lines indicate SSP tracks shaded by the deployment date, and the background colors show August–September 2016 mean satellite sea surface salinity measured with the SMAP satellite. The "x" denotes the position of the SPURS-2 central mooring. Deployment 18, 2016, was made west of the domain at around 9.5°N, 140.5°W. Labeled deployments are discussed in detail in the results. Inset: The black box outlines the area shown in the main plot and colors show mean satellite sea surface salinity.

the rain event, and wind speed (Wijesekera et al. 2003; Asher et al. 2014; Drushka et al. 2016, 2019). The spatial scale of these features, generally on the order of kilometers to tens of kilometers, is the same size as rain cells (Soloviev and Lukas 1996; Wijesekera et al. 1999). Several studies have observed rain-formed fresh lenses in the near-surface ocean, but a smaller number of concurrent observations of turbulence have been made (Brainerd and Gregg 1997; Smyth et al. 1997; Wijesekera et al. 1999; Callaghan et al. 2014; Walesby et al. 2015; Drushka et al. 2016; ten Doeschate et al. 2019). These observations have been made over the lifetime of a few individual fresh lenses and thus do not represent a wide range of wind and rain conditions. It is intuitive that strong turbulence will cause fresh lenses to mix away, and weak turbulence will allow them to persist. Complicating matters, near-surface stratification has been shown to enhance surface currents and turbulence (Wijesekera et al. 1999; Sutherland et al. 2016). Stratification resulting from freshwater input or diurnal warming has also been shown to suppress turbulence beneath the stratified layer (Smyth et al. 1996, 1997; Walesby et al. 2015; Sutherland et al. 2016; Moulin et al. 2018; Wijesekera et al. 2020), as turbulent kinetic energy (TKE) dissipation rates (ε) have been observed to be reduced by up to two orders of magnitude below stratified layers (ten Doeschate et al. 2019). Several previous observations of near-surface salinity anomalies have been made in the western tropical Pacific during rain events associated with westerly wind bursts. These observations indicate that fresh lenses can be quickly advected or mixed downward because of high winds (Brainerd and Gregg 1997; Wijesekera et al. 1999). An objective of the present study was to analyze observations of turbulence across a wide variety of conditions, including the low-wind rain events characteristic of the ITCZ.

Only a limited amount of research has focused on the top meter of the ocean (Brainerd and Gregg 1993, 1997; Wijesekera et al. 1999; Callaghan et al. 2014; Walesby et al. 2015; Sutherland et al. 2016; Moulin et al. 2018; Reverdin et al. 2020). Due to difficulties in measuring in this depth range, few efforts have studied rainfall-enhanced turbulence in the field, and to our knowledge observations of turbulence within fresh lenses have not been previously made shallower than 0.5 m. Laboratory experiments, some of which have observed the top 0.5 m, show that rain and wind can significantly enhance turbulence near the surface (Katsaros and Buettner 1969; Green and Houk 1979; Ho et al. 2004; Zappa et al. 2009; Harrison et al. 2012; Harrison and Veron 2017), with the impact of raindrops elevating ε by varying levels. For instance, in laboratory studies of

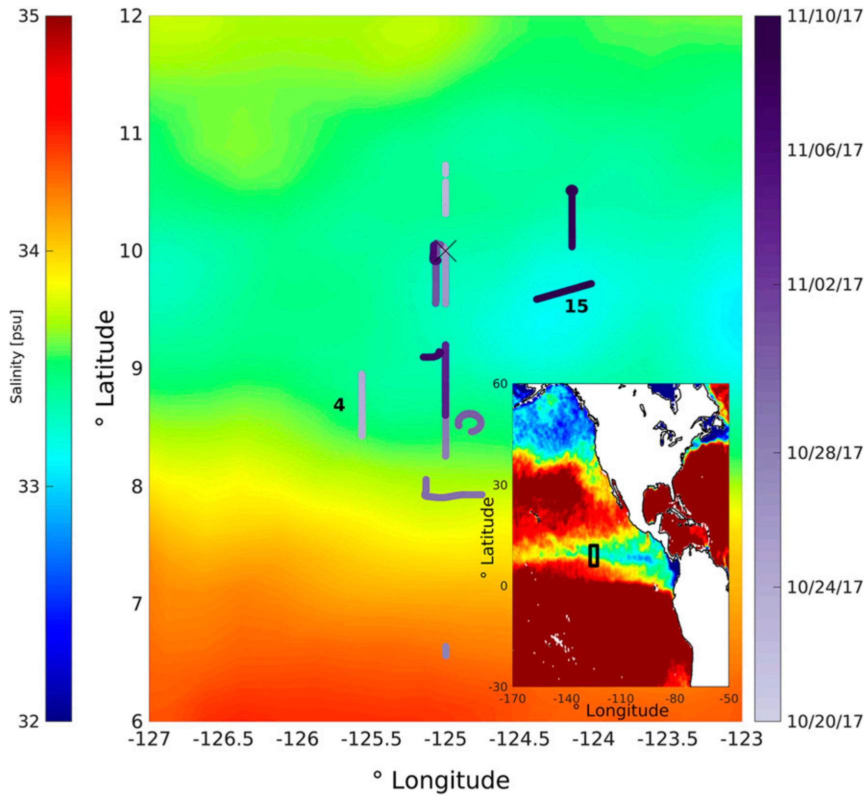

FIG. 2. As in Fig. 1, for the 2017 SPURS-2 cruise deployments. The background colors show October–November 2017 mean sea surface salinity measured by SMAP.

rain on seawater, Harrison and Veron (2017) found that ε was only weakly dependent on rain rate while Zappa et al. (2009) found that raindrops can enhance ε by multiple orders of magnitude in the top 10 cm. Experiments of rain on freshwater (Harrison et al. 2012) and seawater (Zappa et al. 2009) found that this effect was predominately confined to the top 0.3 m. Harrison et al. (2012) determined that rainfall enhanced turbulence during low wind speeds when the ratio of the kinetic energy fluxes of rain (KEF_r) and wind (KEF_w), defined as

$$\beta = \frac{\mathrm{KEF}_r}{\mathrm{KEF}_w}, \quad (1)$$

was greater than 1 (Zappa et al. 2009; Harrison et al. 2012). KEF_r can be estimated as

$$\mathrm{KEF}_r = \frac{1}{2}\rho_d w^2 R, \quad (2)$$

where ρ_d is the density of rainwater, w is the vertical velocity of drops, and R is the rain rate (Ho et al. 1997, 2007; Harrison et al. 2012). KEF_w is defined as

$$\mathrm{KEF}_w = \rho_a\left(\frac{\tau}{\rho_w}\right)^{3/2}, \quad (3)$$

where ρ_a is the density of air, τ is wind stress, and ρ_w is the density of seawater (Ho et al. 2000; Harrison et al. 2012). When $\beta > 1$, rain contributes more to the air–sea kinetic energy flux than wind and therefore rainfall is expected to influence turbulence near the surface (Zappa et al. 2009; Harrison et al. 2012; Harrison and Veron 2017).

The primary data used in this study were collected using a ship-towed, surface-following Surface Salinity Profiler (SSP), which was deployed 34 times for a total of 223 h during the August–September 2016 and October–November 2017 SPURS-2 cruises. Drushka et al. (2019) give a detailed description of the SSP, a modified stand-up paddleboard with an affixed 1.2-m-deep keel. The SSP was towed at speeds of 1–2 m s^{-1} outside of the ship's wake to measure undisturbed water. The SSP had conductivity, temperature, and depth instruments (CTDs) mounted to its keel at 12-, 23-, 54-, and 110-cm depth along with intake hoses designed to measure temperature and salinity in the top 5 cm (hereinafter, referred to as surface measurements). Microstructure temperature (μ_T) and conductivity (μ_C) sensors were mounted at 37-cm depth. The platform followed the swell waves, as evidenced by minimal variance in pressure observations from the CTDs (Drushka et al. 2019): sensor depths generally varied by only ± 3 cm. Iyer et al. (2021) calculated ε from the μ_T observations using a spectral fitting procedure and found that the SSP is an effective platform for measuring ε over large spatial areas. Applying the assumptions of Osborn and Cox (1972) and Osborn (1980), ε is related to the dissipation of temperature variance (χ_T) by

$$\varepsilon = \frac{N^2\chi_T}{2\Gamma\langle dT/dz\rangle^2}, \quad (4)$$

where N is buoyancy frequency, Γ is mixing efficiency, and $\langle dT/dz \rangle$ is the vertical temperature gradient (here, computed between 23- and 54-cm depth; angle brackets denote a 1-min average). The TKE dissipation rate ε was calculated by determining the best-fit Batchelor (1959) spectrum to each observed spectrum (representing 1-min time averages), assuming consistency with the χ_T–ε relation from Eq. (4). Spectral fitting was done following the procedure of Ruddick et al. (2000). A detailed discussion of the data, methods, processing steps, and uncertainty in ε estimates from μ_T data can be found in Iyer et al. (2021).

The μ_T sensor malfunctioned in 2017, so ε was derived from μ_C observations for 16 SSP deployments in 2017 (44% of the total data). To adapt the method of Iyer et al. (2021) to conductivity spectra, we applied the theory presented by Washburn et al. (1996) and Nash and Moum (1999). Conductivity is a function of two correlated variables, temperature T and salinity S, so a conductivity gradient spectrum Ψ_C is equal to the sum of a temperature gradient spectrum Ψ_T, a salinity gradient spectrum Ψ_S, and the T–S cross spectrum Ψ_{TS},

$$\Psi_C(k) = a^2\Psi_S(k) + 2ab\Psi_{TS}(k) + b^2\Psi_T(k), \tag{5}$$

which is expressed as a function of wavenumber k (Nash and Moum 1999). The terms a and b relate T and S variations, respectively, to conductivity variations. For seawater at approximately 33 psu and 25°C, we used $a = 0.019\,70\ \mathrm{S\,m^{-1}\,psu^{-1}}$ and $b = 0.027\,01\ \mathrm{S\,m^{-1}\,K^{-1}}$. The T and S are well correlated (linear coefficients of determination usually exceeded 0.9), which justifies the assumption that the cross spectrum can be defined as

$$\Psi_{TS}(k) = \sqrt{\Psi_T(k)\Psi_S(k)}. \tag{6}$$

We assumed that both Ψ_T and Ψ_S follow the theoretical Batchelor (1959) form. In the viscous–convective and viscous–diffusive subranges, the form of the scalar (T or S; denoted as θ) Batchelor spectrum for isotropic turbulence is (Gibson and Schwarz 1963)

$$\Psi_\theta(k) = \frac{\sqrt{2q}\chi_\theta}{2D_\theta k_b^\theta} f(\alpha_\theta), \tag{7}$$

where

$$f(\alpha_\theta) = \alpha_\theta\left[\exp(-\alpha_\theta^2/2) - \alpha_\theta\int_{\alpha_\theta}^{\infty}\exp(-x^2/2)\,dx\right], \tag{8}$$

$\alpha_\theta = \sqrt{2q}k/k_b^\theta$, q is the Batchelor subrange constant, and D_θ is the diffusivity of heat or salt. We used $q = 3.9$ (Grant et al. 1968), $D_T = 1.49 \times 10^{-7}\ \mathrm{m^2\,s^{-1}}$, and $D_S = 1.50 \times 10^{-9}\ \mathrm{m^2\,s^{-1}}$ (Gill 1982). The Batchelor cutoff wavenumber k_b^θ is defined as

$$k_b^\theta = \left(\frac{\varepsilon}{\nu D_\theta^2}\right)^{1/4} \tag{9}$$

with $\nu = 1 \times 10^{-6}\ \mathrm{m^2\,s^{-1}}$, the kinematic viscosity of seawater (Gill 1982). Following Washburn et al. (1996) and Nash and Moum (1999), the right side of Eq. (5) was rewritten using Eq. (7) in terms of χ_T and χ_S. The term χ_S can further be related to χ_T knowing a local T–S relation (Gregg 1984, 1987):

$$\chi_S = \left(\frac{dS}{dT}\right)^2\chi_T = m^2\chi_T. \tag{10}$$

We estimated m, the slope of the linear T–S curve, using T and S data from the 23- and 54-cm CTDs assuming the relation holds at the spatial scale of turbulent processes near the sea surface. The entire right side of Eq. (5) can then be expressed as a function of only χ_T and ε by substituting Eq. (10) for χ_S. Finally, ε was computed using the same procedure as described by Iyer et al. (2021) for temperature spectra: the Osborn and Cox (1972) assumptions were applied, and iterative spectral fitting was used to determine χ_T and ε.

The μ_C-derived ε (denoted as ε_C) estimates were validated with ε observations from μ_T (denoted as ε_T) in 2016, when both sensors were functional. During 2016, the median and mean differences between ε_C and ε_T were factors of 2.29 and 2.51, respectively (ε_T was higher). This difference was below one order of magnitude 97% of the time (Fig. 3a), which was generally much lower than the uncertainty bounds (typically one to two orders of magnitude; Iyer et al. 2021). The ε_C and ε_T values bin averaged in $1\ \mathrm{m\,s^{-1}}$ wind speed bins were consistent within 95% confidence intervals in all but two wind speed bins (Fig. 3b). A possible cause of the discrepancy between ε_C and ε_T is the assumption of a perfect positive correlation between T and S in calculations of theoretical conductivity spectra. If this correlation were not perfect, the second term on the right side of Eq. (5) would be smaller and therefore theoretical conductivity spectra would be shifted downward for given values of χ_T and ε. As a result, fitting observed conductivity spectra to these theoretical spectra would result in lower values of ε. The discrepancy between ε_C and ε_T was largest when salinity stratification was weak; T and S were very well correlated within fresh lenses. As a result, the vast majority of data with weak stratification is above the 1:1 line on Fig. 3a, while data with stronger stratification generally have a smaller bias between ε_C and ε_T.

In addition to the SSP data, this study uses meteorological measurements including rain rate and wind speed corrected to 10-m height, which were made from ship-based sensors (Clayson et al. 2019). Air–sea heat, moisture, and momentum fluxes were observed using direct covariance techniques (Clayson et al. 2019). These data are available on a 1-min time stamp.

3. Results

A wide range of atmospheric conditions were observed, including low-wind rain events (wind speeds $< 3\ \mathrm{m\,s^{-1}}$) which occur frequently in the eastern tropical Pacific (Yuter and Houze 2000; Wijesekera et al. 2005). We present a series of case studies of rain events to assess the drivers of turbulence that influence fresh lens evolution.

a. *Spatial and temporal variability of salinity, temperature, and TKE dissipation rate during individual rain events*

An intense rain event associated with very low wind speeds and exceptionally large vertical S and T gradients in the upper

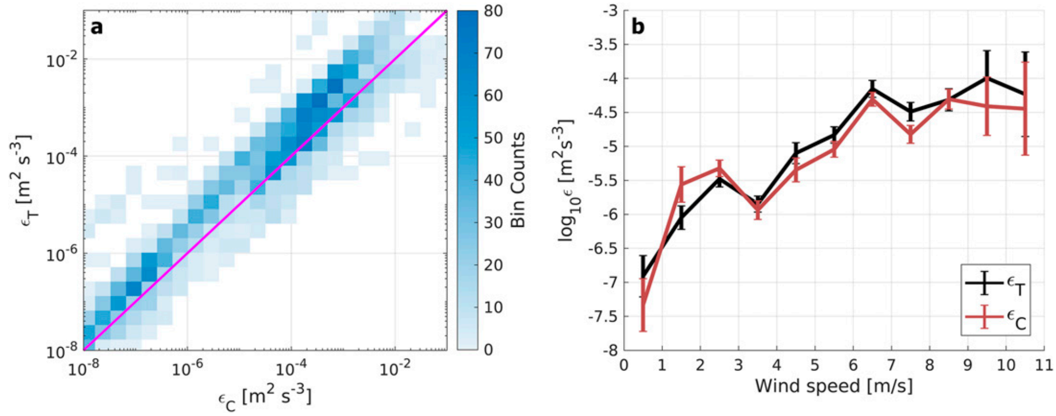

FIG. 3. (a) Binned scatterplot of 1-min ε_C vs ε_T during 2016 SSP deployments when both μ_T and μ_C data were available (total $N = 3373$), (b) binned $\log_{10}\varepsilon_T$ (black) and $\log_{10}\varepsilon_C$ (brown) vs wind speed for 2016 SSP deployments. Wind speed bin width is 1 m s^{-1}, and data points plotted in the center of each bin represent an average of observed 1-min estimates within a wind bin (minimum of 10). Error bars denote 95% confidence intervals (standard error) of the mean value within each bin.

meter occurred on 11 September 2016 (Deployment 13; Fig. 4). When the SSP was deployed around 1240 local time (LT), rain was falling at 10 mm h^{-1} (Fig. 4a) and a rain-formed fresh anomaly was present in the top 54 cm (Fig. 4b). At the beginning of the deployment, the rain rate and vertical S and T gradients in the top 23 cm steadily increased while the wind speeds decreased from 3 to 4 m s^{-1} to under 1 m s^{-1}. Just after 1300 LT, T and S in the top 23 cm increased for a short period of time, possibly due to wind-driven mixing caused by the small spike in wind speed around 1300 LT. At approximately 1320 LT, the maximum S and T stratification in the top 54 cm was observed, with little T or S anomaly at or below 54 cm. At this time, the differences in S and T between the surface and 54 cm ($S_{54\mathrm{cm}} - S_{0\mathrm{cm}}$ and $T_{54\mathrm{cm}} - T_{0\mathrm{cm}}$; hereinafter, subscripts will denote measurement depth) were 10.5 psu and 2°C, respectively (Figs. 4b,c). This stratification maximum occurred when wind speeds were under 1 m s^{-1}. Wind speed and ε were positively correlated during this deployment (Figs. 4a,d). The TKE dissipation rate ε was initially over 10^{-5} m^2 s^{-3}, but decreased to under 10^{-7} m^2 s^{-3} around 1300 LT when salinity stratification increased in the top 54 cm (Fig. 4d). From 1320 until 1350 LT, wind speeds increased to over 8 m s^{-1} while the rain rate was high, varying between 20 and 50 mm h^{-1}. Despite the strong rain, S increased in the upper 23 cm, while $S_{54\mathrm{cm}}$ decreased (Fig. 4b). These changes suggest wind-driven mixing of fresher surface water with saltier water below 54 cm. This is confirmed by a large increase in ε, from 10^{-7} m^2 s^{-3} at 1320 LT to 10^{-3} m^2 s^{-3} at 1410 LT (Fig. 4d). During the second half of the SSP deployment, wind speeds were well over 5 m s^{-1} and ε values were high, roughly varying between 10^{-3} and 10^{-4} m^2 s^{-3}. The small amount of freshwater that fell during this period mixed downward almost immediately and did not form a prominent near-surface lens (Fig. 4b).

Figure 5 shows a prolonged rain event, during which rain occurred in both low and high wind conditions, that was observed on 17 September 2016 (Deployment 18). This deployment was made much farther west than the other deployments (around 9.5°N, 140.5°W), but was still within the ITCZ (Fig. 1). Rainfall varied between 1 and 10 mm h^{-1}, with a few bursts of 10–30 mm h^{-1} rain, for a time period of roughly ten hours (Fig. 5a) when wind speeds varied between 3 and 6 m s^{-1} (Fig. 5a). During this time, T and S in the top meter were weakly stratified (vertical gradients on the order of 0.1 psu m^{-1} and 0.1°C m^{-1}; Figs. 5b,c). From 0630 until 1400 LT, ε usually varied between 10^{-6} and 10^{-5} m^2 s^{-3}, with higher values corresponding to periods of higher wind and heavier rain (e.g., around 0900 LT in Figs. 5a,d). These turbulence levels were large enough to generate some mixing of freshwater, but not large enough to mix freshwater away as soon as it fell, as evidenced by the weak stratification during light rain and slightly stronger stratification during heavier rain. A large fresh anomaly (0.5–1 psu m^{-1} vertical S gradient) was observed in the top meter between 1200 and 1600 LT, although there was not an increase in rain rate or large drop in wind speed around 1200 LT (Fig. 5). A possible explanation for this feature is that heavier rain may have formed the lens before the ship traveled over that area, and winds were low enough that the resulting fresh lens persisted long enough to be captured by the SSP, similar to the observations made by Thompson et al. (2019a). Despite the steady wind speeds, ε had a broad peak from 1300 until 1400 LT of approximately 10^{-5} m^2 s^{-3}. This increase may have been due to the trapping of momentum and resulting enhancement of turbulence in the fresh layer, consistent with Walesby et al. (2015) who observed an enhancement of ε of over one order of magnitude within a 5–10 m thick near-surface fresh layer. Following the small increase in turbulence, ε subsequently decreased to $<10^{-6}$ m^2 s^{-3} around 1400 LT, likely because of a decrease in wind speed to <2 m s^{-1}. From 1415 to 1630 LT, wind speeds increased from <2 to >7 m s^{-1}. This increase in wind speed was accompanied by an increase in ε and a decrease in S and T stratification. We conclude that the increase in wind speed toward the end of the deployment enhanced turbulence in the top meter and mixed the fresh lens into the water column.

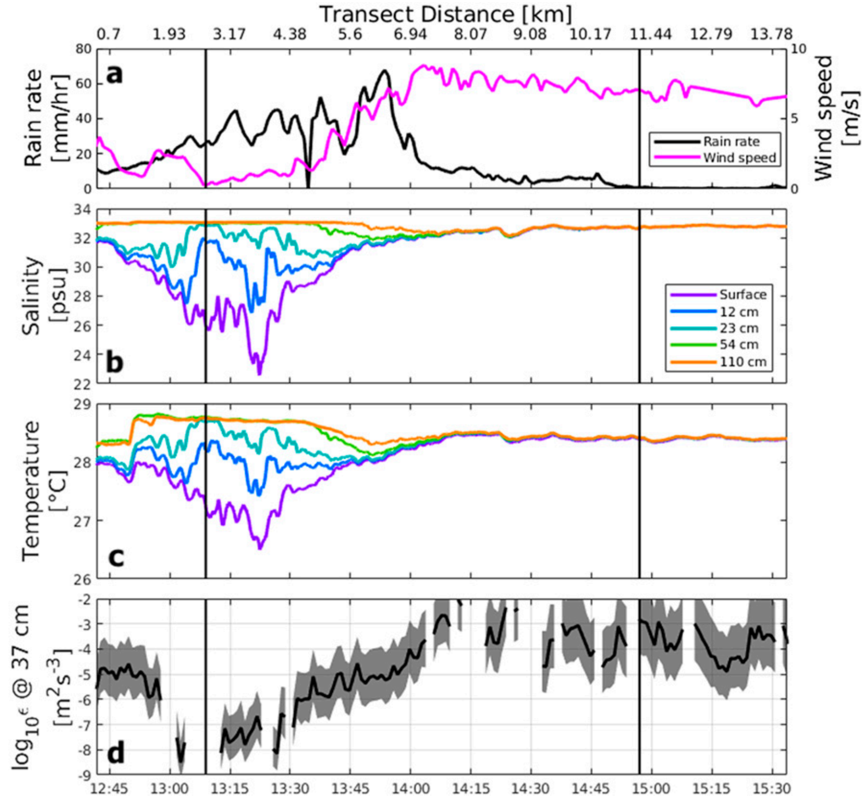

FIG. 4. (a) Rain rate and wind speed measured at the ship, (b) salinity, and (c) temperature at five depths measured by the SSP, (c) 0–110-cm temperature, and (d) $\varepsilon_{37\mathrm{cm}}$ during SSP Deployment 13, 11 Sep 2016. The shaded gray area denotes the uncertainty in estimates of $\varepsilon_{37\mathrm{cm}}$ as explained by Iyer et al. (2021). The bottom x axis shows local time. The top axis shows horizontal SSP transect distance. The black vertical lines denote the times where the SSP crossed over the same geographic location (1309 and 1457 LT); the track is shown in Fig. 10.

A short and intense rain event associated with a squall line was observed during SSP Deployment 15 on 9 November 2017 (Fig. 6). Very light precipitation fell for the first several hours of the deployment, and ε was over $10^{-3}\,\mathrm{m^2\,s^{-3}}$ (Fig. 6d). Vertical gradients in T and S were near zero during this time period. There were significant spatial T and S variations, likely due to fronts or other features that were encountered as the ship moved southwest in a straight line over a 50-km distance (Fig. 2). Heavier rainfall started just after 1900 LT, reached a maximum rain rate of over $10\,\mathrm{mm\,h^{-1}}$ around 1930 LT, and weakened to under $2\,\mathrm{mm\,h^{-1}}$ before 2000 LT (Fig. 6a). During the peak in rainfall around 1915 LT, sustained wind speeds were around $10\,\mathrm{m\,s^{-1}}$. Average vertical T and S gradients in the top 110 cm were only 0.027°C $\mathrm{m^{-1}}$ and 0.073 psu $\mathrm{m^{-1}}$ immediately following the rain event (Figs. 6b,c). The high sustained wind speeds generated near-surface mixing, as can be seen from the high ε values, which mixed freshwater downward. As a result, only weak stratification developed in the top meter following rain; instead, the fresh lens extended deeper (Figs. 6b,d). For the most part, ε decreased steadily throughout the deployment from 10^{-2} to $10^{-4}\,\mathrm{m^2\,s^{-3}}$ and did not correlate with wind speed, in contrast to the observed low-wind rain events (Figs. 4 and 5). The high observed ε may have been a result of the enhancement of turbulence beneath breaking waves, as wind speeds were $>5\,\mathrm{m\,s^{-1}}$ throughout most of the deployment: whitecapping from breaking waves is often observed above wind speeds of 4–5 $\mathrm{m\,s^{-1}}$ and increases greatly with increasing wind speeds (Callaghan et al. 2008; Schwendeman and Thomson 2015). Because wave data were not available, we cannot definitively confirm that wave breaking enhanced ε. Much of the ε data in the first 3 h of the time series were rejected because ε values were unreasonable ($>10^{-1}\,\mathrm{m^2\,s^{-3}}$), possibly due to contamination of the measurements by bubbles (Iyer et al. 2021): during active wave-breaking, bubbles can significantly affect μ_C observations in the top few meters (Soloviev and Lukas 2003). A decrease in ε of two orders of magnitude, and a sharp decrease in salinity in the upper meter, was observed for 15 min immediately following the rain event despite a $5\,\mathrm{m\,s^{-1}}$ increase in wind. The decrease in ε may have been the result of stratification inhibiting the downward transfer of momentum for this short period of time.

A period of diurnal warming, interspersed with several rain events, was observed during SSP Deployment 4 on 24 October 2017 (Fig. 7). Temperature T increased by 0.5°C in the top 23 cm from 0930 to 1300 LT (Fig. 7c), as a result of morning

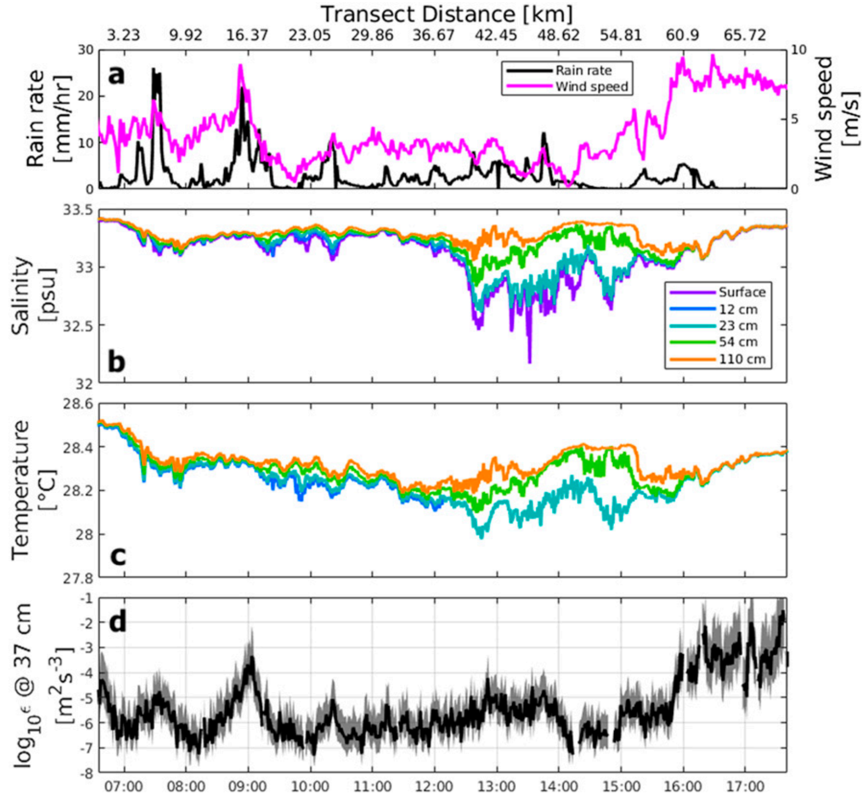

FIG. 5. As in Fig. 4, for SSP Deployment 18, 17 Sep 2016. Wind speed and ε_{37cm} data are also shown in Fig. 5 of Iyer et al. (2021). Surface temperature data were not available for this deployment.

solar heating. When this diurnal warm layer was present, ε was around $10^{-7}\,m^2\,s^{-3}$, roughly two orders of magnitude lower than the average ε observed during the remainder of the deployment (Fig. 7d). A brief rain event at 1100 LT was associated with a peak rain rate of nearly $20\,mm\,h^{-1}$ and a decrease in wind speed to $2\,m\,s^{-1}$. This was the only instance of rain falling on a strong diurnal warm layer in the SSP data. The rain event formed a thin (<23 cm thick) fresh lens around 1100 LT. Despite weak winds, the rain event coincided with the destruction of stratification from diurnal warming and a significant increase in ε (Figs. 7c,d). Increased turbulence may partly have resulted from increased cloud cover and decreased solar radiation destabilizing the near-surface layer prior to the strong rainfall, leading to weaker density stratification compared to the preceding and following periods of diurnal warming. In addition, during the period of stronger rainfall, cool rainwater input destroyed the remaining T stratification, so surface stratification was not sufficiently strong to trap momentum and suppress turbulence at 37 cm. Variable winds associated with the rain event before the ship passed through, and the direct impact of raindrops on the sea surface may have also contributed to the enhanced turbulence levels at 1100 LT. Wind speeds were variable between 3 and $5\,m\,s^{-1}$ for the first 6 h of the deployment until about 1530 LT (Fig. 7a). The large and intense rain event observed just before 1600 LT was associated with rain rates of over $50\,mm\,h^{-1}$ and a wind speed maximum of $8\,m\,s^{-1}$. The high winds likely caused ε to increase after 1600 LT to over $10^{-5}\,m^2\,s^{-3}$ through wind-driven mixing and probably wave breaking (Figs. 7a,d): wave breaking was often visually observed at wind speeds above 6–$7\,m\,s^{-1}$. Because of the high turbulence levels, the rain-formed fresh lens was mixed away quickly and little stratification remained in the top meter immediately after the large rain event ended.

b. *Synthesis of measurements*

The case studies show a range of behavior of turbulence and stratification in response to different rain and wind conditions. To gain insight into the drivers of near-surface ε during rain events, we compared observations of ε, binned by wind speed, to expected values of ε for a theoretical law of the wall boundary layer. Within a ''law of the wall'' layer, ε scales inversely with depth (Dillon et al. 1981; Soloviev et al. 1988) and depends only on wind stress and depth (here depth is taken as 37 cm, the average depth of the microstructure probes). We also made comparisons with the wind- and wave breaking-dependent observational scalings suggested by Terray et al. (1996) and Esters et al. (2018). Because direct wave measurements are not available at the ship and SSP's location, we generally describe waves in the region using data from the SPURS-2 central mooring and the observational scalings. Specifically, we used the same wave parameters as Iyer et al. (2021) to calculate the Esters et al. (2018) and Terray et al. (1996)

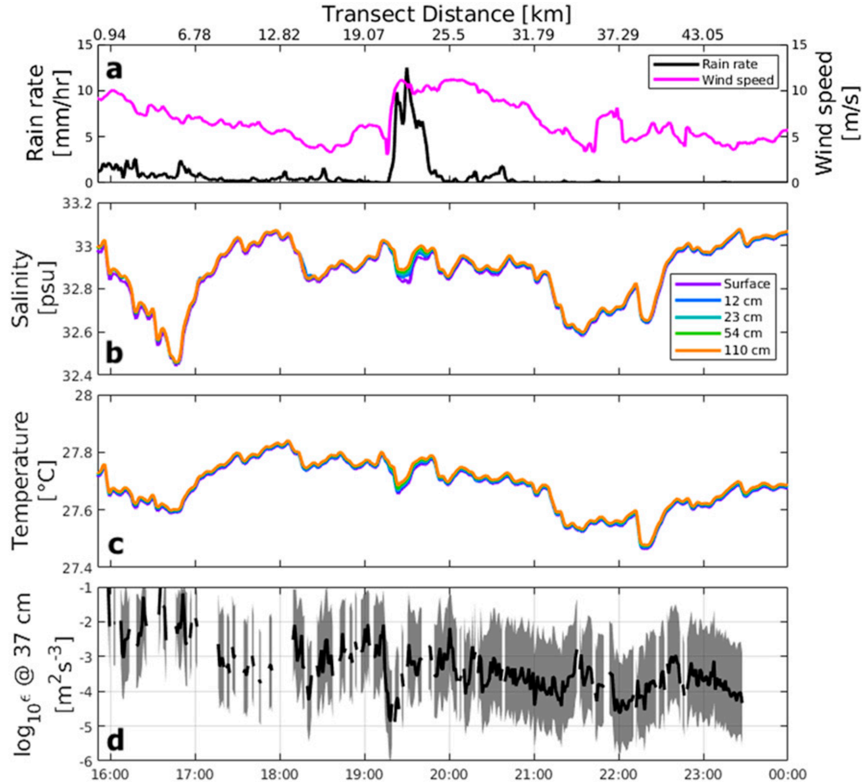

FIG. 6. As in Fig. 4, for SSP Deployment 15, 9 Nov 2017.

scalings: H_s was assumed to be between 0 and 3.0 m (consistent with SPURS-2 central mooring wave observations; wave data available from NOAA NDBC Station 43010, owned and maintained by WHOI). Effective wave speed and wave ages suggested by Esters et al. (2018) and Terray et al. (1996) were used for each respective scaling (shown in Fig. 8 and subsequent figures). These choices, wave observations during SPURS-2, and potential inconsistencies between SSP observations and the scalings are discussed in greater detail by Iyer et al. (2021).

Figure 8 shows bin-averaged ε for four different rain and stratification conditions. In almost all conditions, there was a statistically significant increase in ε with increasing wind speed, and ε was generally consistent with the scalings of Terray et al. (1996) and Esters et al. (2018). However, for a given wind speed, ε was spread over a large range of values for different rain and stratification conditions. This suggests a complex interplay between wind, waves, rain, stratification, and mixing. These relationships will be investigated in the following section.

c. *The influence of rain and stratification on TKE dissipation rate*

To unravel the effects of rain and stratification on turbulence, ε data were subdivided based on near-surface vertical S and T gradients, rain rate, and β. We defined conditions of stratification based on $T_{54\mathrm{cm}} - T_{12\mathrm{cm}}$ (denoted as dT) and $S_{54\mathrm{cm}} - S_{12\mathrm{cm}}$ (denoted as dS). The 12–54-cm depth range was chosen to capture stratification at depths around or above the 37-cm depth of the microstructure sensors. The β value was calculated from Eqs. (1)–(3) assuming that $w = 9\,\mathrm{m\,s^{-1}}$ for all cases. The vast majority (95%) of tropical raindrops have diameters greater than 0.6 mm (Thompson et al. 2015), and therefore would be associated with terminal velocities of approximately $9 \pm 0.25\,\mathrm{m\,s^{-1}}$ (Lhermitte 1988; Ho et al. 2004). We defined four mutually exclusive sets of conditions. Low stratification without significant rainfall (Fig. 8, black; 90.3% of data) was defined as having $dS < 0.005$ psu, $-0.05° < dT < 0.05°$C, and $\beta < 1$. S stratification (Fig. 8, pink; 5.5% of data), which occurred during and after rainfall while fresh lenses persisted, was defined as having $dS > 0.05$ psu. Diurnal warming-generated stratification (Fig. 8, orange; 2.9% of data) was defined as daytime (local time between 0600 and 1800 LT) data when the rain rate was under $1\,\mathrm{mm\,h^{-1}}$, $dS < 0.05$ psu, and $dT < -0.05°$C. Low stratification with significant rainfall (Fig. 8, blue; 1.3% of data) was defined as having $\beta > 1$, a rain rate of over $10\,\mathrm{mm\,h^{-1}}$, $dS < 0.05$ psu, and $-0.05° < dT < 0.05°$C.

Figure 8 provides insight into the effect of stratification on ε during different wind speed regimes. At wind speeds $< 2\,\mathrm{m\,s^{-1}}$, ε was over one order of magnitude lower when rain-induced S stratification was present (pink line) compared to conditions of low stratification and $\beta < 1$ (black line), likely because stratification above 37 cm suppresses ε at 37 cm (hereinafter, referred to as $\varepsilon_{37\mathrm{cm}}$) when wind speeds are low. Stratified layers generated by diurnal warming and rain have been associated with suppressed turbulence at depths between

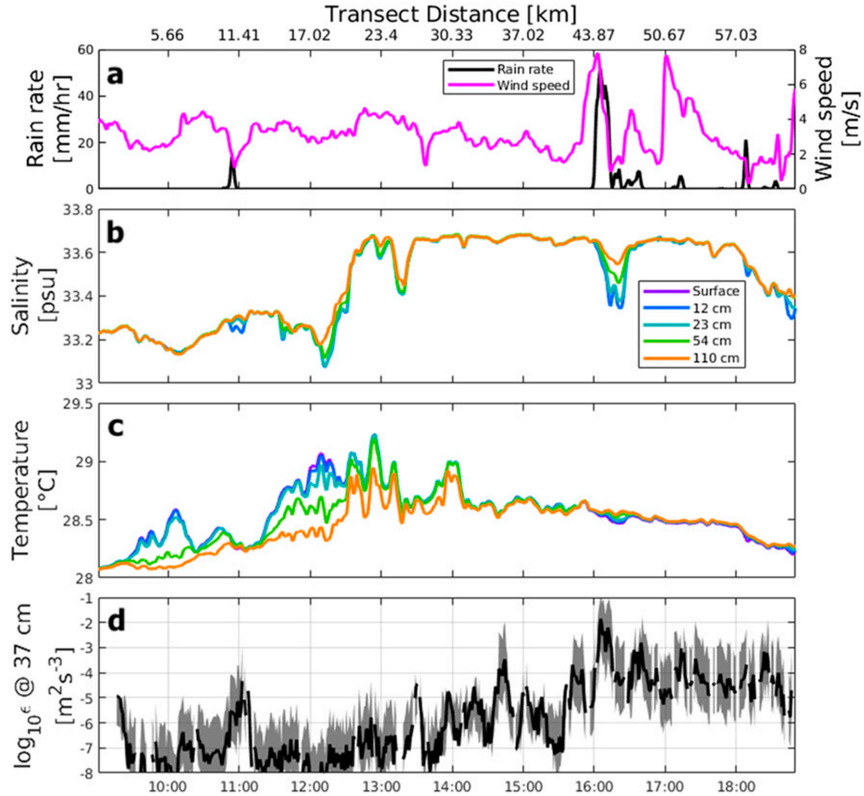

FIG. 7. As in Fig. 4, for SSP Deployment 4, 24 Oct 2017.

1 and 10 m, and it has been hypothesized that stratification inhibits the downward transfer of turbulent energy (Brainerd and Gregg 1993; Smyth et al. 1997; Moulin et al. 2018; ten Doeschate et al. 2019; Wijesekera et al. 2020). To our knowledge, this is the first evidence from field observations that even very thin (<0.5 m) stratified near-surface layers can suppress turbulence at deeper levels. Harrison and Veron (2017) observed a similar effect at shallow depths in a laboratory experiment. The effect of rain-generated stratified layers suppressing turbulence at low wind speeds is illustrated by several individual cases. For instance, Fig. 9b shows a fresh lens that was associated with significant stratification above 37 cm. The ε_{37cm} was roughly equal to the law of the wall values during this period (Fig. 9d). Once wind speeds increased and caused the near-surface stratification to mix away (at around 1850 LT), ε_{37cm} increased to the levels predicted by the Esters et al. (2018) and Terray et al. (1996) scalings.

When wind speeds were above $3\,m\,s^{-1}$, ε_{37cm} was not suppressed during rain-induced stratification (Fig. 8). When stratification was present at wind speeds between 4 and $5\,m\,s^{-1}$, ε_{37cm} was slightly elevated, although this increase was not statistically significant. Elevated ε_{37cm} at moderate winds (4–$5\,m\,s^{-1}$) may occur because winds generate enough mixing that freshwater penetrates deeper than 37 cm. Therefore, we observed enhanced (rather than suppressed) turbulence because the microstructure sensors were within (and not below) the stratified surface layer. Salinity S stratification was not observed at wind speeds over $8\,m\,s^{-1}$ (pink line in Fig. 8) because at higher wind speeds, freshwater from rain was immediately transported downward due to wind-driven mixing.

The blue line in Fig. 8 shows ε_{37cm} for cases with low stratification, $\beta > 1$, and rain rate above $10\,mm\,h^{-1}$–in other words, conditions with high winds when salinity stratification was mixed away immediately during strong rain (e.g., 1930 LT in Fig. 6). These conditions occurred only when wind speeds were above $5\,m\,s^{-1}$ because at lower wind speeds, rain rates of $10\,mm\,h^{-1}$ generated greater amounts of stratification. In these cases, ε_{37cm} was enhanced compared to nonraining and unstratified conditions. This suggests that rain enhances turbulence at wind speeds of 5–$10\,m\,s^{-1}$ when $\beta > 1$. In contrast, Harrison et al. (2012) found from laboratory experiments of rainfall over freshwater that as winds increase above $3.5\,m\,s^{-1}$, the direct effects of rain on turbulence deeper than the top few centimeters become minimized. Our results differ from those of Harrison et al. (2012) because their freshwater experiments did not account for salinity stratification following rain; we found that significant salinity stratification (which was present only at wind speeds under $5\,m\,s^{-1}$) masked the direct impact of rain on ε_{37cm}. Our findings are generally consistent with the effect of stratification discussed by the saltwater laboratory study of Harrison and Veron (2017), who considered only the top 10 cm.

d. The influence of diurnal warming on TKE dissipation rate

Several diurnal warming events were observed during the SSP deployments (e.g., Fig. 7). Observed ε_{37cm} values during

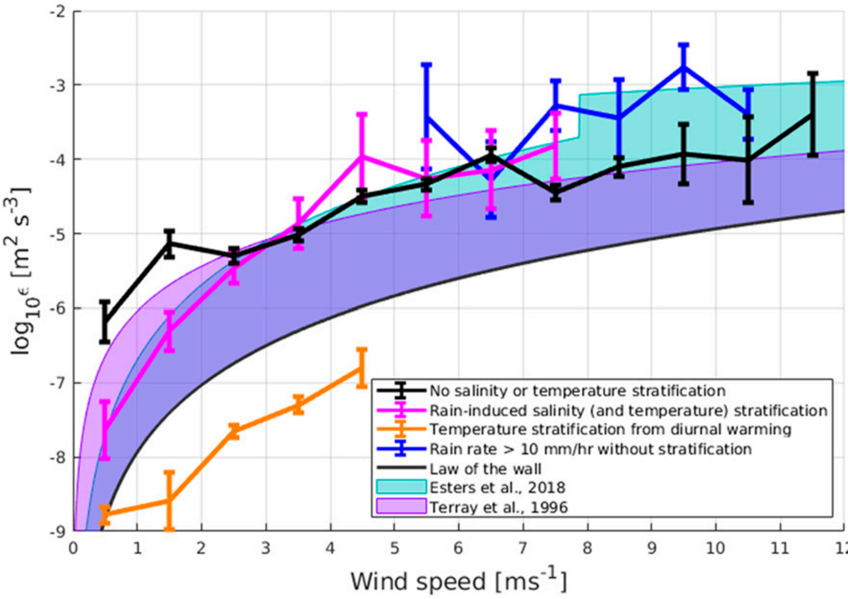

FIG. 8. Binned $\log_{10}\varepsilon$ vs wind speed for all SSP deployments, where $\varepsilon_{37\mathrm{cm}}$ data have been subdivided by stratification and rain conditions. Bins and error bars specifications are the same as Fig. 3b. Conditions with little T or S stratification and $\beta < 1$ are shown in black, conditions of salinity stratification are shown in pink, conditions of diurnal warming are shown in orange, and conditions of strong rainfall without stratification are shown in blue. The criteria for categorizing these data are discussed in section 3c; each category is mutually exclusive. Wave-dependent scalings, assuming significant wave heights between 0 and 3.0 m, as suggested by Terray et al. (1996) and Esters et al. (2018), are shown by the purple and light blue shadings, respectively. The step change in the Esters et al. (2018) scaling results from assuming a linear, piecewise wave age (Wang and Huang 2004). The theoretical law of the wall $\log_{10}\varepsilon_{37\mathrm{cm}}$ is shown by the gray line (lower bound of the shaded region).

near-surface diurnal warming were roughly two orders of magnitude lower than conditions of low stratification and well below the Terray et al. (1996) and Esters et al. (2018) scalings and the law of the wall (orange line in Fig. 8). The suppression of turbulence within diurnal warm layers is consistent with previous observations: Moulin et al. (2018) observed suppressed turbulent dissipation rates of up to two orders of magnitude following sunrise in the tropical ocean. Our definition of diurnal warming, requiring $dT < -0.05°\mathrm{C}$, only captures events with significant amounts of T stratification above the 37 cm microstructure sensor, and excludes conditions of rain-induced T stratification. We infer that the low $\varepsilon_{37\mathrm{cm}}$ during diurnal warming conditions is a result of stratification above this depth that inhibits the downward transfer of turbulent energy. This is the same mechanism that causes suppressed turbulence below rain-formed fresh lenses.

It is intuitive to expect similar levels of turbulence suppression whether stratification is caused by S or T. However, we observed significantly lower $\varepsilon_{37\mathrm{cm}}$ in conditions of diurnal warming than in S-stratified conditions caused by rain. We hypothesize that this is due to two mechanisms: the time scale of stratified layer persistence and raindrop impacts. During SSP deployments, T-stratified layers persisted for 54 min on average, compared to 23 min for S-stratified layers (defining persistence time as when stratification existed before and after 30 min of unstratified conditions). We note that these values are constrained by the times and lengths of SSP deployments. Previous studies have shown that diurnal warm layers are associated with daily cycles of mixed layer ε of one to two orders of magnitude (Sutherland et al. 2016; Moulin et al. 2018; Pujiana et al. 2018; Wijesekera et al. 2020), whereas we observed that fresh lenses often lasted for only a short period of time and sometimes did not significantly influence $\varepsilon_{37\mathrm{cm}}$ (e.g., before 1100 LT in Fig. 5). Because of this, S stratification may not have as significant of an effect on $\varepsilon_{37\mathrm{cm}}$ compared to T stratification. We also hypothesize that $\varepsilon_{37\mathrm{cm}}$ is elevated in S-stratified conditions due to raindrop impacts. Section 3c shows that the effect of stratification suppressing $\varepsilon_{37\mathrm{cm}}$ is dominant over the enhancement of $\varepsilon_{37\mathrm{cm}}$ from raindrop impacts at low wind speeds, but it is possible that raindrop impacts influence $\varepsilon_{37\mathrm{cm}}$ in fresh lenses not confined to the very surface (e.g., after 1200 LT in Fig. 5). Specifically, at low wind speeds in Fig. 8, the pink line (S stratification, usually during rain) is below the black line (no stratification) because stratification inhibits turbulence, but above the orange line (diurnal warming) because of the long persistence of diurnal warm layers and effect of raindrop impacts on $\varepsilon_{37\mathrm{cm}}$. The small sample size of diurnal warming events (only 2.9% of data) and uncertainty due to the methods used to calculate $\varepsilon_{37\mathrm{cm}}$ (discussed by Iyer et al. 2021) may also have

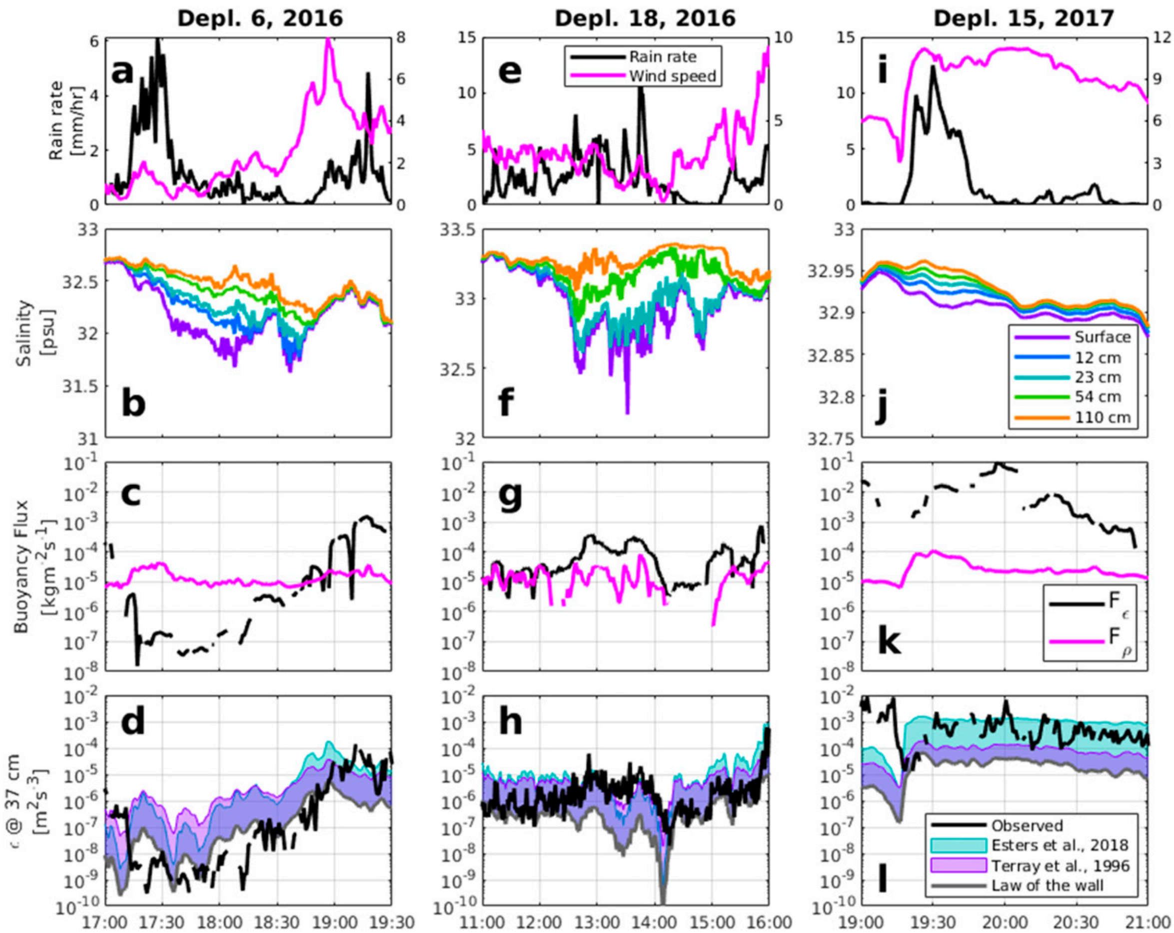

FIG. 9. (a),(e),(i) Rain rate and wind speed; (b),(f),(j) salinity from the SSP; (c),(g),(k) downward air–sea buoyancy flux (F_ρ) and 37-cm turbulent buoyancy flux smoothed with a 10-min moving mean (F_ε); and (d),(h),(l) $\varepsilon_{37\mathrm{cm}}$ during three rain events occurring on (left) 31 Aug 2016 (Deployment 6), (center) 17 Sep 2016 (Deployment 18), and (right) 9 Nov 2017 (Deployment 15). Turbulence scalings shown follow the color scheme of Fig. 8.

contributed to the differences between $\varepsilon_{37\mathrm{cm}}$ in S- and T-stratified conditions.

4. Discussion

Because wind is a strong driver of turbulence near the surface, wind speed was positively correlated with $\varepsilon_{37\mathrm{cm}}$ (Fig. 8). Rain was also shown to influence $\varepsilon_{37\mathrm{cm}}$ through two opposing mechanisms. First, when winds are too weak to break down stratification following rain, $\varepsilon_{37\mathrm{cm}}$ is suppressed. Second, raindrop impacts directly enhance $\varepsilon_{37\mathrm{cm}}$, consistent with laboratory studies (Zappa et al. 2009; Harrison et al. 2012; Harrison and Veron 2017). At low wind speeds under $3\,\mathrm{m\,s^{-1}}$, the suppressing effect of stratification dominates over the enhancing effect of raindrops (Fig. 8). Despite this, raindrop impacts still contribute to turbulence above the depth of the microstructure sensors. Previous research also demonstrates that raindrop impacts enhance gas exchange at the air–sea interface (Ho et al. 2000, 2004, 2007; Zappa et al. 2009; Harrison et al. 2012; Harrison and Veron 2017).

Rain-formed fresh lenses can immediately be mixed downward or advected away when wind speeds are high (e.g., Fig. 6), or persist for several hours under low-wind conditions (e.g., Fig. 5). A major complication to understanding the dynamics of fresh lenses is the fact that turbulence both controls and is affected by near-surface stratification. In the case of long-lasting fresh lenses during low wind conditions, lenses persist because ε is low. However, near-surface stratification within lenses may also inhibit turbulent mixing below due to the trapping of momentum (Smyth et al. 1996, 1997; Moulin et al. 2018; ten Doeschate et al. 2019). In other words, low turbulence both enables and is a result of the persistence of fresh lenses in low-wind conditions. The fresh lens persisting from 1230 until 1500 LT during Deployment 18, 2016, demonstrates this (Fig. 5). This lens was associated with steady or increasing $\varepsilon_{37\mathrm{cm}}$ during the beginning of its lifetime (1230–1300 LT) when wind speeds were relatively constant or decreasing, which suggests that momentum was trapped near the surface and thus that turbulence was elevated within a surface layer that included the microstructure sensors. The $\varepsilon_{37\mathrm{cm}}$ only decreased around 1400 LT when wind speeds decreased to under $2\,\mathrm{m\,s^{-1}}$.

Both wind and the stratification within lenses influence ε, but it is difficult to determine the relative effect of each of these two processes in driving turbulence within the very near-surface layer. Our results suggest that in areas where low-wind rain is frequent, or significant near-surface diurnal warming occurs, stratification is an important factor that can influence ε by up to several orders of magnitude.

The observations made in this study were collected from a moving ship. This further complicates the results because the data were influenced by both spatial and temporal variability. Observed changes in S, T, and ε can be thought of as representing variations in either space or time, but in reality, variability existed in both space and time. Most of the deployments lasted several hours, with the ship covering well over 50 km of horizontal distance during the longest deployments (Figs. 1 and 2). The observed oceanic conditions could be influenced by recent local atmospheric conditions before the ship traveled over that area, in addition to observed atmospheric conditions. As described in section 3, Deployment 18, 2016, is an example of a case where recent local forcing had a major influence on the salinity signal measured by the SSP. In cases where wind speeds were high enough to mix freshwater down quickly, the ocean responded locally to the observed atmospheric conditions; Figs. 4 and 10 demonstrate this. The SSP was towed over the same location twice during Deployment 13, 2016, at 1309 and 1457 LT (Fig. 10). At 1309 LT, a very strong fresh lens was observed, and the stratification and low winds resulted in very low near-surface turbulence (Figs. 4a,b,d). At 1457 LT, there was little stratification at the same location, wind speeds were much higher, and $\varepsilon_{37\mathrm{cm}}$ increased by roughly five orders of magnitude. The difference in conditions at the same location provides evidence that the oceanic response to atmospheric variability was fast enough for the observed oceanic conditions to reflect the local atmospheric conditions. Because near-surface currents were generally $<0.3\,\mathrm{m\,s^{-1}}$ and the initial salinity anomaly had a horizontal scale of approximately 7 km (Fig. 10), it is unlikely that the fresh lens was instead advected away between 1309 and 1457 LT.

a. Predicting stratified layers with turbulence observations

To gain further insight into the processes that control the evolution of fresh lenses, we compared the atmospheric-driven surface buoyancy flux with the turbulent buoyancy flux near the surface (at 37-cm depth). Surface buoyancy is controlled by heat and salt fluxes, which are influenced by rainfall, solar heating, longwave radiation, latent and sensible heating, and turbulent mixing. We estimated buoyancy fluxes using measurements of evaporation, precipitation, and net heat flux and applying the methods of Schmitt et al. (1989) and others. Specifically, the air–sea buoyancy flux F_ρ and the turbulent 37-cm buoyancy flux F_ε were calculated from heat and salt fluxes,

$$F_\rho = \rho(AF_{T,\rho} - BF_{S,\rho}), \tag{11}$$

$$F_\varepsilon = \rho(AF_{T,\varepsilon} - BF_{S,\varepsilon}). \tag{12}$$

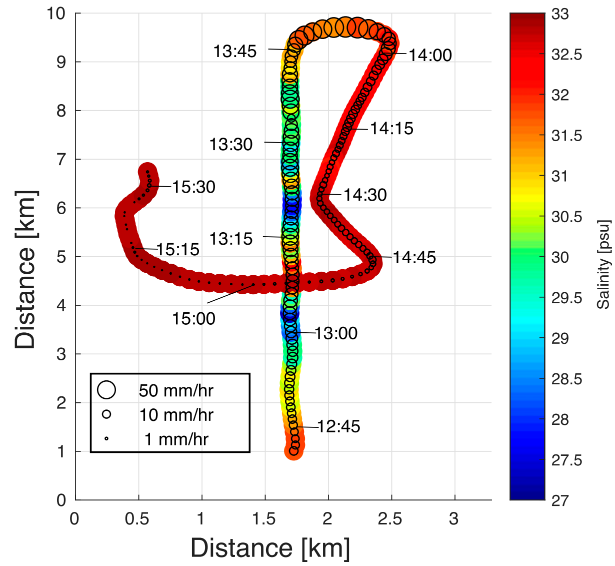

FIG. 10. Spatial location of SSP Deployment 13, 11 Sep 2016. Distance ranges on the map correspond to geographic locations of approximately 8.19°–8.28°N and 125.015°–124.985°W. Circle sizes correspond to rain rates. Colors denote 12-cm salinity measured with the SSP. Time series for this deployment are shown in Fig. 4.

Parameters A and B are the thermal expansion and haline contraction coefficients of seawater, and ρ is the water density. We assumed $A = 3.086 \times 10^{-4}\,°\mathrm{C}^{-1}$ and $B = 7.211 \times 10^{-4}\,\mathrm{psu}^{-1}$, typical of the conditions at the SPURS-2 site. The terms $F_{T,\rho}$ and $F_{S,\rho}$ are the surface heat and salt fluxes, defined as

$$F_{T,\rho} = Q/(\rho C_p), \tag{13}$$

and

$$F_{S,\rho} = (E - R)[S/(1 - S)]. \tag{14}$$

Parameter Q is the net heat flux into the ocean, C_p is the heat capacity of seawater, E is the evaporation rate, and R is the precipitation rate. Turbulent heat and salt fluxes at 37 cm, $F_{T,\varepsilon}$ and $F_{S,\varepsilon}$, were estimated using $\varepsilon_{37\mathrm{cm}}$. We assumed that turbulent heat and salt fluxes are proportional to the eddy diffusivities of heat and salt, respectively, using

$$F_{\theta,\varepsilon} = K_{\theta,\varepsilon}\frac{d\theta}{dz}, \tag{15}$$

where θ is T or S, K_θ is the corresponding eddy diffusivity, and $d\theta/dz$ is the vertical T or S gradient at 37 cm. Diffusivities were calculated by applying the assumptions of Osborn and Cox (1972) using average T and S gradients between the 23- and 54-cm CTDs. This is similar to the method used by Wijesekera et al. (1999). It was expected that $F_\rho > F_\varepsilon$ at 37 cm when fresh lenses were forming or persisting, and that $F_\varepsilon > F_\rho$ when there was little stratification or when fresh lenses were mixing away. In simple intuitive terms, when $F_\rho = F_\varepsilon$, buoyancy entering the surface is exactly balanced by buoyancy being removed through turbulent mixing. Because our turbulent flux estimates

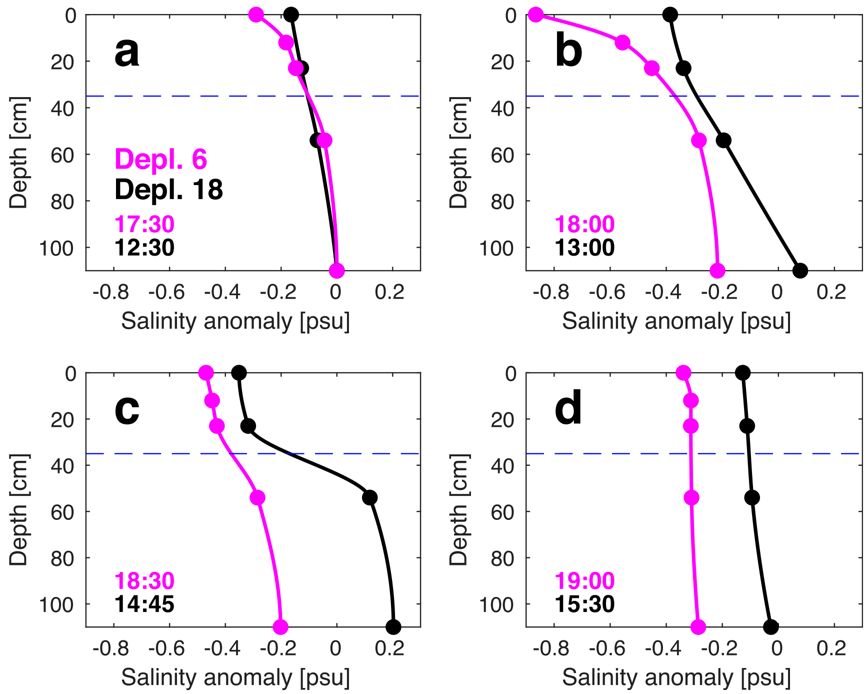

FIG. 11. Salinity anomaly profiles at four points in time during Deployment 6 (pink) and Deployment 18 (black), 2016, corresponding to time series in Figs. 9b and 9j. The 110-cm salinities, from the times denoted in (a), have been subtracted from salinities in all subplots. The dots show measurements from the SSP, and the lines are a cubic interpolation between those measurements. The blue dashed line shows the 37-cm depth of the turbulence estimates. (a) Formation of the fresh lens, (b) maximum salinity gradient, (c) a later time when the lenses are still prominent, and (d) after the lenses have mostly mixed and/or advected away.

were at 37 cm whereas the buoyancy flux was estimated at the sea surface, turbulent mixing and lateral advection that occurred between the surface and 37-cm depth are significant sources of uncertainty.

The flux differences were generally consistent with our expectations: $F_\rho \gg F_\varepsilon$ during and after rain events that produced strong and persistent fresh lenses, as seen in the examples shown in Fig. 9. Deployment 6, 2016, also shown in Fig. 5, was a typical case. From 1700 until 1830 LT, $F_\rho > F_\varepsilon$ by around two orders of magnitude (Fig. 9c). This difference was mostly a result of decreases in F_ε caused by stratification. The fluxes F_ρ and F_ε were roughly equal from 1830 to 1900 LT when light rain fell, wind speeds increased, and $S_{54\mathrm{cm}} - S_{23\mathrm{cm}}$ was large (Figs. 9a–c). After 1930 LT, when $\varepsilon_{37\mathrm{cm}}$ was high, $F_\varepsilon \gg F_\rho$ and the remaining stratification was destroyed.

During rain events that produced fresh lenses that mixed away quickly, F_ρ was often below F_ε. An example of this is the large rain event that was observed during Deployment 15, 2017 (Figs. 6 and 9i–l). Even at the points of maximum rainfall and stratification during this event, $F_\varepsilon \gg F_\rho$ (Fig. 9k). This implies that throughout the rain event, S stratification only occurred while rain continued to be input (Figs. 6b and 9j). That is, freshwater from rain almost immediately mixed away laterally and/or to deeper depths. This is evident from the observed salinities in Fig. 9j: only a very small drop in S (<0.05 psu) was observed near the surface during the rain event despite rain rates over 10 mm h^{-1}.

The ratio of air–sea and turbulent buoyancy fluxes also provides insight into how individual fresh lenses affect turbulent properties near the surface. Rainfall and near-surface vertical S and T gradients were not well correlated across the entire dataset. A comparison of the fresh lenses observed during Deployment 6, 2016, and Deployment 18, 2016, demonstrates this. In both cases, rain fell at 0–10 mm h^{-1}, wind speeds were under 5 m s^{-1} throughout most of the rain event, and fresh lenses having similar vertical S gradients in the upper meter formed (Figs. 9a,b,e,f and 11). During the Deployment 18 event, F_ε almost always exceeded F_ρ (Fig. 9g) and $\varepsilon_{37\mathrm{cm}}$ was enhanced within this fresh lens. In contrast, Fig. 9c shows that $F_\rho > F_\varepsilon$ and $\varepsilon_{37\mathrm{cm}}$ was suppressed (Fig. 9d) during the Deployment 6 event. The differences in turbulence levels between these lenses can be explained by the depths of stratification in the top meter. The top 23 cm were well mixed during Deployment 18 when the fresh lens was strongest (Figs. 9b,f and 11b), likely due to slightly higher wind speeds. Figure 11b shows that the majority of the observed S stratification in the top meter was below the depth of the microstructure sensors within the Deployment 18 lens, but above the depth of the microstructure sensors during the Deployment 6 lens. This, along with the observed turbulence levels, implies that during

Deployment 6, turbulent energy was trapped in a near-surface layer above 37 cm, while during Deployment 18, turbulent energy penetrated to at least 37-cm depth. This point is reinforced by the low $\varepsilon_{37\mathrm{cm}}$ between 1415 and 1500 LT during Deployment 18 (Fig. 9h), when rainfall and low winds generated strong stratification above 37 cm (Fig. 11c). This comparison demonstrates the influence that the depth and strength of rain-formed stratified layers have on near-surface turbulence and that turbulence levels near the surface can differ significantly between rain events that appear similar based on their rain forcing.

The above examples suggest that the difference between the air–sea and turbulent buoyancy fluxes can be used as a predictor of whether a fresh lens will form (or persist). To assess this, we examined whether the presence of stratified layers was related to the difference between the air–sea and turbulent buoyancy flux. Conditions of $N > 0.02\,\mathrm{s}^{-1}$ between 23- and 54-cm depth were used as an indicator of the presence of a stratified layer near the surface. This classification includes prominent fresh lenses and excludes the majority of diurnal warming events, which were typically characterized by $N \le 0.01\,\mathrm{s}^{-1}$. When $F_\varepsilon > F_\rho$, $N < 0.02\,\mathrm{s}^{-1}$ 76% of the time, i.e., stratified layers were observed 24% of the time (Fig. 12). When $F_\rho > F_\varepsilon$, stratified layers were observed 68% of the time. Similar quantitative results were obtained when stratified layers were classified based on N computed between several different depth ranges in the top meter. These results indicate that the downward air–sea buoyancy flux drives the formation of stratified layers, and wind-driven turbulent processes in the top meter contribute to the destruction (and/or advection) of these layers. Highly stratified conditions ($N > 0.1\,\mathrm{s}^{-1}$), indicative of fresh lenses with strong vertical S gradients, were present much more often when $F_\rho > F_\varepsilon$ (14% of data) than when $F_\varepsilon > F_\rho$ (3% of data; Fig. 12). The difference between F_ρ and F_ε appears to be a useful predictor of whether a stratified layer will form during rain. Exceptions, when F_ε exceeded F_ρ but stratification was present, may be the result of uncertainty in the $\varepsilon_{37\mathrm{cm}}$ estimates, the leniency of the $0.02\,\mathrm{s}^{-1}$ stratification criterion, and data collected when turbulence was strong but fresh lenses had not yet mixed away.

b. *Predicting stratified layers with wind speed*

We also evaluated whether atmospheric parameters and air–sea buoyancy fluxes can be used to predict near-surface buoyancy-driven stratification using the relation developed by Thompson et al. (2019b), which incorporates the air–sea surface buoyancy flux and wind speed. A form of this relation modified to incorporate F_ρ is

$$U_s \le \left[\frac{4.02(zF_\rho)}{\rho_{\mathrm{sw}}}\left(\frac{C_D\rho_{\mathrm{air}}}{\rho_{\mathrm{sw}}}\right)^{2/3}\right]^{1/3}, \qquad (16)$$

where U_s is the stable layer wind limit, or the maximum wind speed at which we would expect stratification to occur at depth z. However, we note that Thompson et al. (2019b) developed this relation for $z > 5$ m so it is unclear whether it holds near the surface at $z = 0.37$ m as used here. The terms ρ_{air} and ρ_{sw} are the densities of air and seawater, calculated using the

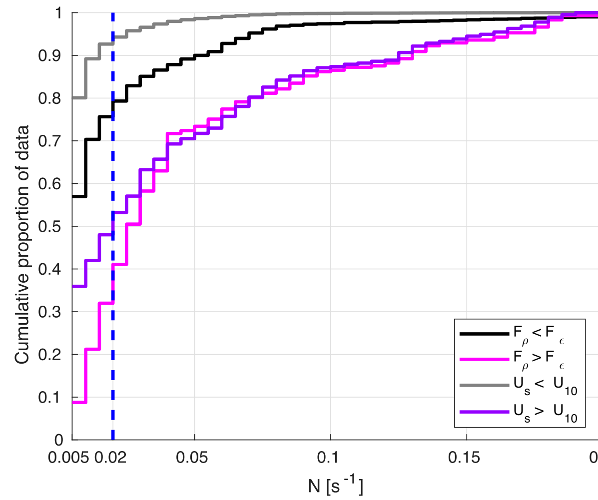

FIG. 12. Cumulative distribution functions of buoyancy frequency during periods of time when the 37-cm turbulent buoyancy flux F_ε exceeded the downward air–sea buoyancy flux F_ρ, (black); $F_\rho > F_\varepsilon$ (pink); when the observed wind speed (U_{10}) exceeded U_s (gray); and when $U_s > U_{10}$ (purple). The y axis shows the proportion of data points that were within or below a particular $0.005\,\mathrm{s}^{-1}$ wide range of N. Each line represents the cumulative proportion of points within only one individual classification, not over a larger set of data. The black and gray lines are analogous (represent conditions where we would expect no near-surface stratification) and the pink and purple lines are analogous (represent conditions where we would expect a near-surface stratified layer). All data collected in 2016 and 2017 when $N > 0.005\,\mathrm{s}^{-1}$ are shown. The dashed blue line ($N > 0.02\,\mathrm{s}^{-1}$) indicates the threshold used to identify fresh lenses.

approximate mean densities at the SPURS-2 study site of 1.24 and 1020 kg m^{-3}, and C_D is the drag coefficient, taken as 0.9×10^{-3}. As with the previous comparison, N between the 23- and 54-cm CTDs was used as an indicator of the presence of a near-surface stratified layer.

We predicted stable layer formation by comparing U_s, calculated with Eq. (16), and observed wind speed. Data were subdivided into two categories: when U_s was greater than the observed wind speed and when U_s was less than the observed wind speed. Stratified layers ($N > 0.02\,\mathrm{s}^{-1}$) formed and persisted much more often when wind speeds were below U_s (52% of the time; purple line in Fig. 12) compared to when wind speeds were above U_s (7% of the time; gray line in Fig. 12). This finding supports the relation developed by Thompson et al. (2019b) as a good predictor of stratified layer formation in the top meter of the ocean. Equation (16) is especially accurate in predicting when stratified layers will not form. As before, the specific predictive accuracies stated are highly dependent on the $N > 0.02\,\mathrm{s}^{-1}$ stratification criterion.

Figure 12 clearly shows that the presence of near-surface fresh lenses can be predicted based on air–sea fluxes and atmospheric or ocean turbulence data. The results shown in Fig. 8 indicate that turbulence in the upper meter can be predicted from wind and wave data using parameterizations such as those used by Terray et al. (1996) and Esters et al. (2018). Given these results, air–sea (F_ρ) and near-surface turbulent (F_ε) buoyancy fluxes, and therefore fresh lens formation and persistence, can in theory be predicted from atmospheric data without near-surface salinity observations. This is a useful finding considering the difficulty in making in situ near-surface measurements.

5. Summary and conclusions

Wind and waves, rain, and stratification are the primary drivers of variability in near-surface turbulence. Rain primarily affects turbulence indirectly through stratification. The direct effect of raindrop impacts on $\varepsilon_{37\mathrm{cm}}$ can be clearly observed in the absence of stratification at wind speeds above 5–6 m s^{-1}, but also likely elevates turbulence at lower wind speeds. When winds were weak (under 3 m s^{-1}), wind-driven turbulent mixing was reduced; as a result, fresh lenses had stronger vertical S and T gradients near the surface. Several cases having enhanced $\varepsilon_{37\mathrm{cm}}$ within a fresh lens were observed, consistent with previous studies of thicker fresh lenses (e.g., Smyth et al. 1997; ten Doeschate et al. 2019) and demonstrating the codependence of near-surface S, T, and turbulence. When rain-induced stratification was present below the depth of the microstructure sensors and winds were moderate or high, fresh lenses did not suppress $\varepsilon_{37\mathrm{cm}}$. The ratio of the downward air–sea buoyancy flux and the turbulent buoyancy flux is a reasonable predictor of fresh lens formation and persistence. An empirical relation incorporating the air–sea buoyancy flux and wind speed developed by Thompson et al. (2019b) was also found to accurately predict fresh lens formation. These findings indicate that near-surface salinity and turbulence can potentially be predicted from atmospheric observations made in situ from ships or moorings or remotely using satellites. However, we note that satellite observations of rain represent both spatial and temporal averages and do not have high enough spatial or temporal resolution to accurately observe the small-scale intense rain events that were observed during SPURS-2 (Thompson et al. 2019a). Resolving this discrepancy warrants further research.

A significant limitation to our results is that observations of ε were only made at 37-cm depth. This is shallow enough to observe the effects of near-surface stratification and raindrop impacts on turbulence, but likely is too deep to measure processes within fresh lenses that have significant stratification above this (e.g., Fig. 4). Presumably, enhanced (suppressed) ε would be observed above (within) shallow stratified layers in the same manner as for deeper lenses. Raindrop impacts on ε would also be stronger closer to the surface (Zappa et al. 2009; Harrison et al. 2012). We recommend that future work include additional ε measurements at a shallower depth (5–20 cm). This would further elucidate the competing roles of raindrop impacts and stratification on turbulence, and provide insight into the depths at which each of these processes have a significant impact. We also suggest future studies utilize additional observations to disentangle the influence of spatial and temporal variability of ε within stratified layers, as observations of S, T, and ε often showed patterns that suggest a significant role of horizontal processes (e.g., Fig. 4). Spatial and temporal variations could be isolated using observations from a mooring, drifters, or autonomous vehicles.

The connections between rain, wind, waves, the evolution of fresh lenses, and near-surface turbulence are crucial for our understanding of the transfer of freshwater from rainfall to the larger-scale salinity structure of the ocean. This is especially important in regions such as the ITCZ, where the input of freshwater to the ocean by rain is large, but patchy because of the small scale of rain events. The relationships between wind, rain, and turbulence explored in this study can potentially improve existing model parameterizations of air–sea interaction, and will be useful in investigations of the larger-scale connections between atmospheric forcing and the near-surface salinity structure.

Acknowledgments. SSP and meteorological data from the SPURS-2 cruises are available at NASA PO.DAAC (Drushka 2019; Clayson 2019). Wave data from the central mooring are available on the NOAA NDBC site at https://www.ndbc.noaa.gov/station_page.php?station=43010. The SMAP (Soil Moisture Active Passive) Sea Surface Salinity data (Level 3, Version 4.0; Fore et al. 2016) used in Figs. 1 and 2 was obtained from the NASA JPL EOSDIS PO.DAAC. We thank the scientists, captain, and crew on the 2016 and 2017 SPURS-2 cruises on the R/V *Roger Revelle* for their assistance in collecting much of the data. We acknowledge James Edson (WHOI) and Carol Anne Clayson (WHOI) for providing and processing the meteorological data (wind speed, rain rate, air–sea fluxes) for both the 2016 and 2017 SPURS-2 cruises. We thank Dan Clark (APL-UW) for engineering the SSP and collecting SSP data. We acknowledge Elizabeth Thompson (NOAA) for valuable input and collecting and processing SSP CTD data. We acknowledge William Asher, Andrew Jessup, and Trina Litchendorf for collecting SSP data. We are thankful for code and several valuable suggestions from Luc Rainville. Some of the spectral fitting code was modified from code provided by Barry Ruddick. This work was supported by NSF Grant OCE-1458759 and NASA Grants NNX15AF68G and 80NSSC18K1499. We thank two anonymous reviewers for insightful comments and suggestions that greatly improved the manuscript.

REFERENCES

Asher, W. E., A. T. Jessup, R. Branch, and D. Clark, 2014: Observations of rain-induced near-surface salinity anomalies. *J. Geophys. Res. Oceans*, **119**, 5483–5500, https://doi.org/10.1002/2014JC009954.

Batchelor, G. K., 1959: Small-scale variation of convected quantities like temperature in turbulent fluid Part I. General discussion and the case of small conductivity. *J. Fluid Mech.*, **5**, 113–133, https://doi.org/10.1017/S002211205900009X.

Boyer, T. P., S. Levitus, J. I. Antonov, R. A. Locarnini, and H. E. Garcia, 2005: Linear trends in salinity for the world ocean, 1955–1998. *Geophys. Res. Lett.*, **32**, L01604, https://doi.org/10.1029/2004GL021791.

Brainerd, K. E., and M. C. Gregg, 1993: Diurnal restratification and turbulence in the oceanic surface mixed layer: 1. Observations. *J. Geophys. Res.*, **98**, 22 645–22 656, https://doi.org/10.1029/93JC02297.

——, and ——, 1997: Turbulence and stratification on the tropical ocean-global atmosphere-coupled ocean-atmosphere response experiment microstructure pilot cruise. *J. Geophys. Res.*, **102**, 10 437–10 455, https://doi.org/10.1029/96JC03864.

Callaghan, A. H., G. de Leeuw, L. Cohen, and C. D. O'Dowd, 2008: Relationship of oceanic whitecap coverage to wind speed and wind history. *Geophys. Res. Lett.*, **35**, L23609, https://doi.org/10.1029/2008GL036165.

——, B. Ward, and J. Vialard, 2014: Influence of surface forcing on near-surface and mixing layer turbulence in the tropical Indian Ocean. *Deep-Sea Res. I*, **94**, 107–123, https://doi.org/10.1016/j.dsr.2014.08.009.

Cifelli, R., S. Nesbitt, S. Rutledge, W. Petersen, and S. Yuter, 2007: Radar characteristics of precipitation features in the EPIC and TEPPS regions of the east Pacific. *Mon. Wea. Rev.*, **135**, 1576–1595, https://doi.org/10.1175/MWR3340.1.

——, ——, ——, ——, and ——, 2008: Diurnal characteristics of precipitation features over the tropical East Pacific: A comparison of the EPIC and TEPPS regions. *J. Climate*, **21**, 4068–4086, https://doi.org/10.1175/2007JCLI2020.1.

Clayson, C. A., 2019: SPURS-2 Research vessel meteorological series data for the E. Tropical Pacific field campaign R/V Revelle cruises, version 1.0. PO.DAAC, accessed 27 April 2020, https://doi.org/10.5067/SPUR2-MET00.

——, J. B. Edson, A. Paget, R. Graham, and B. Greenwood, 2019: Effects of rainfall on the atmosphere and the ocean during SPURS-2. *Oceanography*, **32**, 86–97, https://doi.org/10.5670/oceanog.2019.216.

Dillon, T. M., J. G. Richman, C. G. Hansen, and M. D. Pearson, 1981: Near-surface turbulence measurements in a lake. *Nature*, **290**, 390–392, https://doi.org/10.1038/290390a0.

Drushka, K., 2019: SPURS-2 Towed surface salinity profile (SSP) data for the E. Tropical Pacific R/V Revelle cruises, version 1.0. PO.DAAC, accessed 31 January 2021, https://doi.org/10.5067/SPUR2-SSP00.

——, W. E. Asher, B. Ward, and K. Walesby, 2016: Understanding the formation and evolution of rain-formed fresh lenses at the ocean surface. *J. Geophys. Res. Oceans*, **121**, 2673–2689, https://doi.org/10.1002/2015JC011527.

——, ——, A. T. Jessup, E. Thompson, S. Iyer, and D. Clark, 2019: Capturing fresh lenses with the surface salinity profiler. *Oceanography*, **32**, 76–85, https://doi.org/10.5670/oceanog.2019.215.

Durack, P. J., 2015: Ocean salinity and the global water cycle. *Oceanography*, **28**, 20–31, https://doi.org/10.5670/oceanog.2015.03.

——, S. E. Wijffels, and R. J. Matear, 2012: Ocean salinities reveal strong global water cycle intensification during 1950 to 2000. *Science*, **336**, 455–458, https://doi.org/10.1126/science.1212222.

Esters, L., Ø. Breivik, S. Landwehr, A. ten Doeschate, G. Sutherland, K. H. Christensen, J.-R. Bidlot, and B. Ward, 2018: Turbulence scaling comparisons in the ocean surface boundary layer. *J. Geophys. Res. Oceans*, **123**, 2172–2191, https://doi.org/10.1002/2017JC013525.

Fairall, C. W., E. F. Bradley, D. P. Rogers, J. B. Edson, and G. S. Young, 1996: Bulk parameterization of air-sea fluxes for tropical ocean-global atmosphere coupled-ocean atmosphere response experiment. *J. Geophys. Res.*, **101**, 3747–3764, https://doi.org/10.1029/95JC03205.

Fore, A. G., S. H. Yueh, W. Tang, B. W. Stiles, and A. K. Hayashi, 2016: Combined active/passive retrievals of ocean vector wind and sea surface salinity with smap. *IEEE Trans. Geosci. Remote Sens.*, **54**, 7396–7404, https://doi.org/10.1109/TGRS.2016.2601486.

Gibson, C. H., and W. H. Schwarz, 1963: The universal equilibrium spectra of turbulent velocity and scalar fields. *J. Fluid Mech.*, **16**, 365–384, https://doi.org/10.1017/S0022112063000835.

Gill, A. E., 1982: *Atmosphere-Ocean Dynamics*. International Geophysics Series, Academic Press, 662 pp.

Grant, H. L., B. A. Hughes, W. M. Vogel, and A. Moilliet, 1968: The spectrum of temperature fluctuations in turbulent flow. *J. Fluid Mech.*, **34**, 423–442, https://doi.org/10.1017/S0022112068001990.

Green, T., and D. F. Houk, 1979: The mixing of rain with near-surface water. *J. Fluid Mech.*, **90**, 569–588, https://doi.org/10.1017/S0022112079002408.

Gregg, M. C., 1984: Entropy generation in the ocean by small-scale mixing. *J. Phys. Oceanogr.*, **14**, 688–711, https://doi.org/10.1175/1520-0485(1984)014<0688:EGITOB>2.0.CO;2.

——, 1987: Diapycnal mixing in the thermocline: A review. *J. Geophys. Res.*, **92**, 5249–5286, https://doi.org/10.1029/JC092iC05p05249.

Harrison, E. L., and F. Veron, 2017: Near-surface turbulence and buoyancy induced by heavy rainfall. *J. Fluid Mech.*, **830**, 602–630, https://doi.org/10.1017/jfm.2017.602.

——, ——, D. T. Ho, M. C. Reid, P. Orton, and W. R. McGillis, 2012: Nonlinear interaction between rain-and wind-induced air-water gas exchange. *J. Geophys. Res.*, **117**, C03034, https://doi.org/10.1029/2011JC007693.

Ho, D. T., L. F. Bliven, R. Wanninkhof, and P. Schlosser, 1997: The effect of rain on air-water gas exchange. *Tellus*, **49B**, 149–158, https://doi.org/10.3402/tellusb.v49i2.15957.

——, W. E. Asher, L. F. Bliven, P. Schlosser, and E. L. Gordan, 2000: On mechanisms of rain-induced air-water gas exchange. *J. Geophys. Res.*, **105**, 24 045–24 057, https://doi.org/10.1029/1999JC000280.

——, C. J. Zappa, W. R. McGillis, L. F. Bliven, B. Ward, J. W. H. Dacey, P. Schlosser, and M. B. Hendricks, 2004: Influence of rain on air-sea gas exchange: Lessons from a model ocean. *J. Geophys. Res.*, **109**, C08S18, https://doi.org/10.1029/2003JC001806.

——, F. Veron, E. Harrison, L. F. Bliven, N. Scott, and W. R. McGillis, 2007: The combined effect of rain and wind on air–water gas exchange: A feasibility study. *J. Mar. Syst.*, **66**, 150–160, https://doi.org/10.1016/j.jmarsys.2006.02.012.

Iyer, S., K. Drushka, and L. Rainville, 2021: Estimating turbulent kinetic energy dissipation rate using microstructure data from the ship-towed Surface Salinity Profiler. *J. Atmos. Oceanic Technol.*, **38**, 77–89, https://doi.org/10.1175/JTECH-D-20-0002.1.

Katsaros, K., and K. J. K. Buettner, 1969: Influence of rainfall on temperature and salinity of the ocean surface. *J. Appl. Meteor.*, **8**, 15–18, https://doi.org/10.1175/1520-0450(1969)008<0015:IOROTA>2.0.CO;2.

Lhermitte, R. M., 1988: Observation of rain at vertical incidence with a 94 GHz Doppler radar: An insight on Mie scattering. *Geophys. Res. Lett.*, **15**, 1125–1128, https://doi.org/10.1029/GL015i010p01125.

Lindstrom, E. J., J. B. Edson, J. J. Schanze, and A. Y. Shcherbina, 2019: SPURS-2: Salinity processes in the upper-ocean regional study 2. The eastern equatorial Pacific experiment. *Oceanography*, **32**, 15–19, https://doi.org/10.5670/oceanog.2019.207.

Moulin, A. J., J. N. Moum, and E. L. Shroyer, 2018: Evolution of turbulence in the diurnal warm layer. *J. Phys. Oceanogr.*, **48**, 383–396, https://doi.org/10.1175/JPO-D-17-0170.1.

Nash, J. D., and J. N. Moum, 1999: Estimating salinity variance dissipation rate from conductivity microstructure measurements. *J. Atmos. Oceanic Technol.*, **16**, 263–274, https://doi.org/10.1175/1520-0426(1999)016<0263:ESVDRF>2.0.CO;2.

Nesbitt, S. W., R. Cifelli, and S. A. Rutledge, 2006: Storm morphology and rainfall characteristics of trmm precipitation features. *Mon. Wea. Rev.*, **134**, 2702–2721, https://doi.org/10.1175/MWR3200.1.

Osborn, T. R., 1980: Estimates of the local rate of vertical diffusion from dissipation measurements. *J. Phys. Oceanogr.*, **10**, 83–89, https://doi.org/10.1175/1520-0485(1980)010<0083:EOTLRO>2.0.CO;2.

——, and C. S. Cox, 1972: Oceanic fine structure. *Geophys. Astrophys. Fluid Dyn.*, **3**, 321–345, https://doi.org/10.1080/03091927208236085.

Price, J. F., 1979: Observations of a rain-formed mixed layer. *J. Phys. Oceanogr.*, **9**, 643–649, https://doi.org/10.1175/1520-0485(1979)009<0643:OOARFM>2.0.CO;2.

Pujiana, K., J. N. Moum, and W. D. Smyth, 2018: The role of turbulence in redistributing upper-ocean heat, freshwater, and momentum in response to the mjo in the equatorial indian ocean. *J. Phys. Oceanogr.*, **48**, 197–220, https://doi.org/10.1175/JPO-D-17-0146.1.

Reverdin, G., A. Supply, K. Drushka, E. Thompson, W. Asher, and A. Lourenço, 2020: Intense and small freshwater pools from rainfall investigated during SPURS-2 on November 9 2017 in the eastern tropical Pacific. *J. Geophys. Res. Oceans*, **125**, e2019JC015558, https://doi.org/10.1029/2019JC015558.

Ruddick, B., A. Anis, and K. Thompson, 2000: Maximum likelihood spectral fitting: The Batchelor spectrum. *J. Atmos. Oceanic Technol.*, **17**, 1541–1555, https://doi.org/10.1175/1520-0426(2000)017<1541:MLSFTB>2.0.CO;2.

Schmitt, R. W., P. S. Bogden, and C. E. Dorman, 1989: Evaporation minus precipitation and density fluxes for the North Atlantic. *J. Phys. Oceanogr.*, **19**, 1208–1221, https://doi.org/10.1175/1520-0485(1989)019<1208:EMPADF>2.0.CO;2.

Schwendeman, M., and J. Thomson, 2015: Observations of whitecap coverage and the relation to wind stress, wave slope, and turbulent dissipation. *J. Geophys. Res. Oceans*, **120**, 8346–8363, https://doi.org/10.1002/2015JC011196.

Smyth, W. D., D. Hebert, and J. N. Moum, 1996: Local ocean response to a multiphase westerly wind burst: 2. Thermal and freshwater responses. *J. Geophys. Res.*, **101**, 22 513–22 533, https://doi.org/10.1029/96JC02006.

——, P. O. Zavialov, and J. N. Moum, 1997: Decay of turbulence in the upper ocean following sudden isolation from surface forcing. *J. Phys. Oceanogr.*, **27**, 810–822, https://doi.org/10.1175/1520-0485(1997)027<0810:DOTITU>2.0.CO;2.

Soloviev, A. V., and R. Lukas, 1996: Observation of spatial variability of diurnal thermocline and rain-formed halocline in the western Pacific warm pool. *J. Phys. Oceanogr.*, **26**, 2529–2538, https://doi.org/10.1175/1520-0485(1996)026<2529:OOSVOD>2.0.CO;2.

——, and ——, 2003: Observation of wave-enhanced turbulence in the near-surface layer of the ocean during TOGA COARE. *Deep-Sea Res. I*, **50**, 371–395, https://doi.org/10.1016/S0967-0637(03)00004-9.

——, N. V. Vershinsky, and V. A. Bezverchnii, 1988: Small-scale turbulence measurements in the thin surface layer of the ocean. *Deep-Sea Res.*, **35A**, 1859–1874, https://doi.org/10.1016/0198-0149(88)90113-6.

SPURS-2 Planning Group, 2015: From salty to fresh—Salinity Processes in the Upper-ocean Regional Study-2 (SPURS-2): Diagnosing the physics of a rainfall-dominated salinity minimum. *Oceanography*, **28**, 150–159, https://doi.org/10.5670/oceanog.2015.15.

Sutherland, G., L. Marié, G. Reverdin, K. H. Christensen, G. Broström, and B. Ward, 2016: Enhanced turbulence associated with the diurnal jet in the ocean surface boundary layer. *J. Phys. Oceanogr.*, **46**, 3051–3067, https://doi.org/10.1175/JPO-D-15-0172.1.

ten Doeschate, A., G. Sutherland, H. Bellenger, S. Landwehr, L. Esters, and B. Ward, 2019: Upper ocean response to rain observed from a vertical profiler. *J. Geophys. Res. Oceans*, **124**, 3664–3681, https://doi.org/10.1029/2018JC014060.

Terray, E. A., M. A. Donelan, Y. C. Agrawal, W. M. Drennan, K. K. Kahma, A. J. Williams, P. A. Hwang, and S. A. Kitaigorodskii, 1996: Estimates of kinetic energy dissipation under breaking waves. *J. Phys. Oceanogr.*, **26**, 792–807, https://doi.org/10.1175/1520-0485(1996)026<0792:EOKEDU>2.0.CO;2.

Thompson, E. J., S. A. Rutledge, B. Dolan, and M. Thurai, 2015: Drop size distributions and radar observations of convective and stratiform rain over the equatorial Indian and west Pacific Oceans. *J. Atmos. Sci.*, **72**, 4091–4125, https://doi.org/10.1175/JAS-D-14-0206.1.

——, W. E. Asher, A. T. Jessup, and K. Drushka, 2019a: High resolution rain maps from an X-band marine radar. *Oceanography*, **32**, 58–65, https://doi.org/10.5670/oceanog.2019.213.

——, J. N. Moum, C. W. Fairall, and S. A. Rutledge, 2019b: Wind limits on rain layers and diurnal warm layers. *J. Geophys. Res. Oceans*, **124**, 897–924, https://doi.org/10.1029/2018JC014130.

Tomczak, M., 1995: Salinity variability in the surface layer of the tropical western Pacific Ocean. *J. Geophys. Res.*, **100**, 20 499–20 515, https://doi.org/10.1029/95JC01544.

Walesby, K., J. Vialard, P. J. Minnett, A. H. Callaghan, and B. Ward, 2015: Observations indicative of rain-induced double diffusion in the ocean surface boundary layer. *Geophys. Res. Lett.*, **42**, 3963–3972, https://doi.org/10.1002/2015GL063506.

Wang, W., and R. X. Huang, 2004: Wind energy input to the surface waves. *J. Phys. Oceanogr.*, **34**, 1276–1280, https://doi.org/10.1175/1520-0485(2004)034<1276:WEITTS>2.0.CO;2.

Washburn, L., T. F. Duda, and D. C. Jacobs, 1996: Interpreting conductivity microstructure: Estimating the temperature variance dissipation rate. *J. Atmos. Oceanic Technol.*, **13**, 1166–1188, https://doi.org/10.1175/1520-0426(1996)013<1166:ICMETT>2.0.CO;2.

Wijesekera, H. W., C. A. Paulson, and A. Huyer, 1999: The effect of rainfall on the surface layer during a westerly wind burst in the western equatorial Pacific. *J. Phys. Oceanogr.*, **29**, 612–632, https://doi.org/10.1175/1520-0485(1999)029<0612:TEOROT>2.0.CO;2.

——, ——, and E. D. Skyllingstad, 2003: Modeling the evolution of a fresh sea surface anomaly produced by tropical rainfall. *J. Geophys. Res.*, **108**, 3338, https://doi.org/10.1029/2002JC001408.

——, D. L. Rudnick, C. A. Paulson, S. D. Pierce, W. S. Pegau, J. Mickett, and M. C. Gregg, 2005: Upper ocean heat and freshwater budgets in the eastern Pacific warm pool. *J. Geophys. Res.*, **110**, C08004, https://doi.org/10.1029/2004JC002511.

——, D. W. Wang, and E. Jarosz, 2020: Dynamics of the diurnal warm layer: Surface jet, high-frequency internal waves, and mixing. *J. Phys. Oceanogr.*, **50**, 2053–2070, https://doi.org/10.1175/JPO-D-19-0285.1.

Yuter, S. E., and R. A. Houze Jr., 2000: The 1997 Pan American climate studies tropical eastern Pacific process study. Part I: ITCZ region. *Bull. Amer. Meteor. Soc.*, **81**, 451–481, https://doi.org/10.1175/1520-0477(2000)081<0451:TPACST>2.3.CO;2.

Zappa, C. J., D. T. Ho, W. R. McGillis, M. L. Banner, J. W. H. Dacey, L. F. Bliven, B. Ma, and J. Nystuen, 2009: Rain-induced turbulence and air-sea gas transfer. *J. Geophys. Res.*, **114**, C07009, https://doi.org/10.1029/2008JC005008.